# Structural Insights into BET Client Recognition of Endometrial and Prostate Cancer-Associated SPOP Mutants

**Michael Sebastian Ostertag[1,2,†], Wiebke Hutwelker[3,4,†], Oliver Plettenburg[3,4], Michael Sattler[1,2] and Grzegorz Maria Popowicz[1,2]**

*1 - **Institute of Structural Biology,** Helmholtz Zentrum München, Ingolstädter Landstr. 1, 85764 Neuherberg, Germany*
*2 - **Center for Integrated Protein Science Munich at Chair of Biomolecular NMR Spectroscopy,** Department Chemie, Technische Universität München, Lichtenbergstrasse 4, 85747 Garching, Germany*
*3 - **Institute of Medicinal Chemistry,** Helmholtz Zentrum München, Ingolstädter Landstr. 1, 85764 Neuherberg, Germany*
*4 - **Institute of Organic Chemistry,** Leibniz Universität Hannover, Schneiderberg 1b, 30167 Hannover, Germany*

***Correspondence to Michael Sattler and Grzegorz Maria Popowicz:** Institute of Structural Biology, Helmholtz Zentrum München, Ingolstädter Landstr. 1, 85764 Neuherberg, Germany. sattler@helmholtz-muenchen.de, grzegorz.popowicz@helmholtz-muenchen.de*
https://doi.org/10.1016/j.jmb.2019.04.017
***Edited by Georg Schulz***

## Abstract

BET proteins such as BRD3 are oncogenic transcriptional coactivators. SPOP binding triggers their proteasomal degradation. In both endometrial and prostate cancers, SPOP mutations occur in the MATH domain, but with opposed influence on drug susceptibility. In prostate cancer, SPOP mutations presumably cause increased BET levels, decreasing BET inhibitor drug susceptibility. As opposed, in endometrial cancer, decreased BET levels concomitant with higher BET inhibitor drug susceptibility were observed. Here, we present the to our knowledge first co-crystal structure of SPOP and a bromodomain containing protein (BRD3). Our structural and biophysical data confirm the suggested loss-of-function in prostate cancer-associated SPOP mutants and provide mechanistic explanation. As opposed to previous literature, our data on endometrial cancer-associated SPOP mutants do not show altered binding behavior compared to wild-type SPOP, indicating a more complex regulatory mechanism. SPOP mutation screening may thus be considered a valuable personalized medicine tool for effective antitumor therapy.



The bromodomain and extraterminal (BET) family of proteins (BRD2, BRD3, BRD4 and BRDT) are involved in various cellular processes, including the modulation of gene expression. Bromodomain containing proteins read acetylation patterns on histones and recruit other protein machinery to regulate gene transcription. As changes in normal histone modification patterns are frequent in cancer, BET proteins seem to be involved in the epigenetic regulation of cancer [1]. As they are able to sustain malignant transcriptional programs in tumors, they were found to be attractive therapeutic targets [2]. Cellular BET levels are regulated through their interaction with the speckle-type POZ protein (SPOP) [2–4], which is part of a cullin-RING-basedE3 ubiquitin–protein ligase complex [5]. In this complex, SPOP serves as the substrate recognition part that directly binds the substrate *via* its MATH domain. SPOP also recognizes CUL3, which binds to an E2 ubiquitin-conjugating enzyme [6]. The E2 enzyme carries activated ubiquitin, which is transferred to the substrate as the signal for proteasomal degradation [7].

SPOP contains a MATH (meprin and TRAF homology) domain (Fig. 1a), which mediates binding of a number of clients [5]. Cancer-genome sequencing studies have shown that in prostate and endometrial cancer the gene encoding the E3-ligase adaptor protein SPOP is frequently mutated [8,9]. SPOP mutations associated with prostate cancer are located in the substrate binding site of the SPOP MATH domain, whereas endometrial cancer-associated mutation sites are found in distant regions of the MATH domain structure [3].

Recently, Janouskova *et al.* [3] reported paradoxical findings, proposing that mutations located in the

 

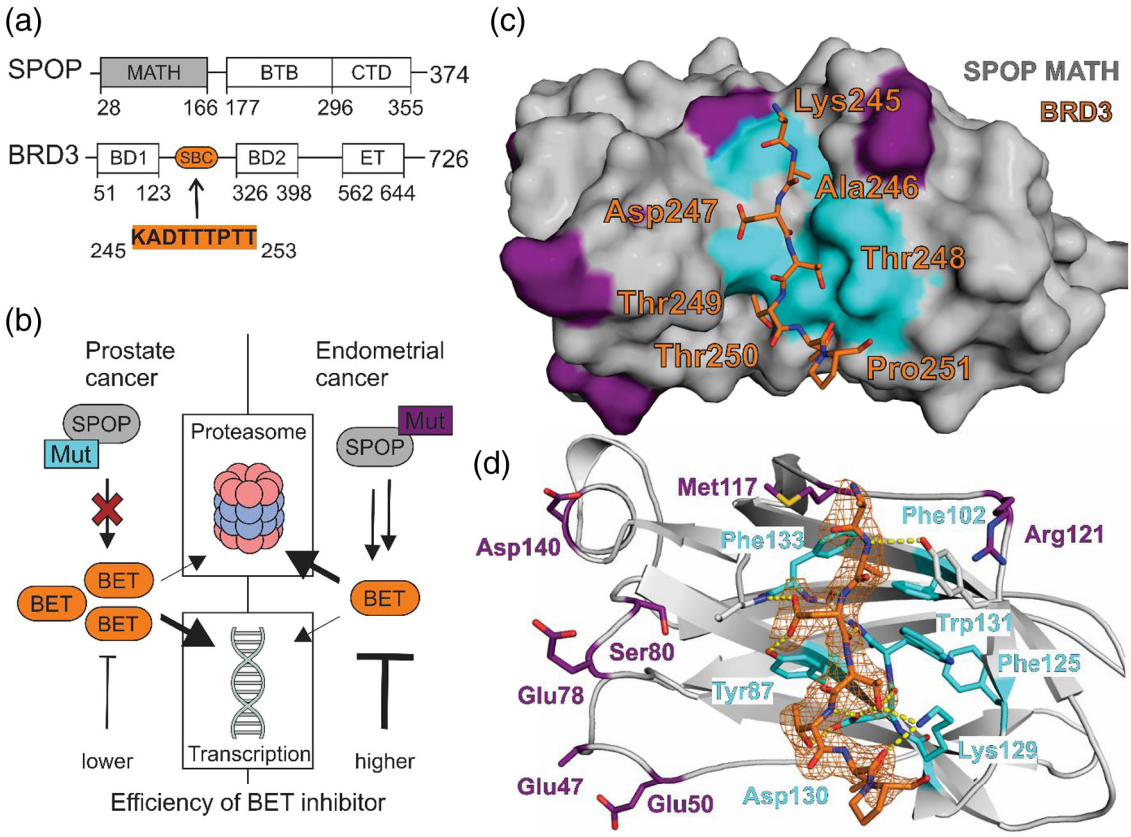


**Fig. 1.** Structure and function of the SPOP–BET complex. (a) Schematic display of SPOP and BRD3 domain architecture. SPOP contains a MATH domain for substrate binding and a BTB domain, which mediates the interaction to the E3 ubiquitin-ligase cullin-3. It also enables dimerization. The C-terminal domain (CTD) contains an additional dimerization interface. BRD3 contains two bromodomains (BD1 and BD2) and the extraterminal (ET) domain. The SPOP binding consensus (SBC; residues 245–253) is located in an unstructured linker region between the two bromodomains. (b) Cellular pathway of the SPOP–BET protein interaction in prostate and endometrial cancer. In prostate cancer, SPOP mutations disrupt BET protein binding, which leads to a decreased ubiquitination turnover and diminished BET degradation by the proteasome. The accumulation of BET proteins causes a malignant transcriptional program with decreased drug susceptibility toward BET inhibitors. Contrarily, in endometrial cancer, cellular BET protein levels are diminished, again leading to a malignant transcriptional program, but increasing the drug susceptibility toward BET inhibitors. Lower BET protein levels are presumably caused by increased SPOP binding due to mutation, resulting in increased ubiquitination and proteasomal degradation rates of BET proteins. (c) Surface display of the SPOP–BRD3 co-crystal structure with BRD3 shown as sticks. SPOP MATH (28–166, wild-type) is shown in gray, and BRD3 (**1**, residues 245–253) is shown in orange. SPOP endometrial cancer-associated mutation sites are shown in purple, and prostate-cancer-associated mutations sites are shown in cyan. BRD3 sits in a shallow groove on the SPOP MATH surface. Prostate cancer-associated mutation sites are clustered around the BRD3 binding site, while endometrial cancer-associated mutation sites are distant from the binding groove. (d) Cartoon display of the SPOP–BRD3 co-crystal structure with key interactions highlighted. Electron density for BRD3 is shown as mesh. Hydrogen bonds between SPOP and BRD3 are shown as yellow dashed lines. Cancer-associated mutation sites and residues involved in binding are shown as sticks. Prostate cancer-associated mutations (cyan) occur in residues directly involved in H-bonds or hydrophobic contacts to the BRD3 ligand, thus disrupting key binding features. This rationalizes the reduced BET protein binding capabilities of prostate cancer-associated SPOP mutants on a structural level.

same SPOP domain lead to opposing effects in drug susceptibility. They showed that BET protein levels are increased in prostate cancer cells carrying typical SPOP mutations. The mutations presumably cause a loss-of-function in SPOP, impairing BET binding and ubiquitination. The subsequent accumulation of BET proteins results in a malignant transcription program and diminished susceptibility of the cancer cells toward small-molecule BET inhibitors (Fig. 1b). As opposed, in endometrial cancer cells, reduced BET protein levels were observed *in vivo*, concomitant with increased drug susceptibility of the cancer cells toward BET inhibitors. The authors suggest a gain-of-function mechanism in endometrial cancer-associated SPOP

mutants, resulting in increased BET protein affinity and ubiquitination [3] (Fig. 1b). However, the molecular mechanisms that might explain this are unclear.

In this study, we characterized the SPOP–BET protein interaction using biophysical *in vitro* techniques such as NMR spectroscopy and isothermal titration calorimetry (ITC). To investigate structural effects of cancer-associated mutations in the SPOP–BET protein interface, we co-crystallized SPOP MATH (residues 28–166) with a peptide comprising the SPOP degron of BRD3 (**1**, residues 245–253, KADTTTPTT). To our knowledge, this represents the first bromodomain-SPOP complex structure. BRD3 was chosen because it has been a focus of study in previous SPOP-related literature [3]. It is representative for the BET protein family as its SPOP binding consensus sequence is identically found in BRD4 and differs from the BRD2 sequence in only one position. The co-crystal structure of SPOP–BRD3 (Fig. 1c) shows that prostate cancer-associated SPOP mutation sites are located directly in the BRD3 binding groove, while endometrial cancer-associated mutation sites are distant from the binding site. A detailed view of the interactions formed between SPOP and BRD3 (Fig. 1d) shows that prostate cancer-associated mutation sites are found in SPOP residues involved in critical interactions with BRD3. SPOP Asp130, for example, forms hydrogen bonds to BRD3 and was previously shown to be critically involved also in SPOP binding to other substrates [10]. In addition, aromatic SPOP residues such as Phe133 and Phe102 form a hydrophobic pocket on the SPOP surface, which is occupied by BRD3 Ala246 and is considered critical for binding. Based on our structure, it is reasonable that the introduction of any prostate cancer-associated SPOP mutation causes significantly weaker BRD3 binding. In contrast, all endometrial cancer-associated SPOP mutation sites are located at positions distant from the BRD3 binding site. Thus, a possible influence on SPOP–BRD3 binding of these mutations needs to be further elucidated.

For a qualitative comparison of BRD3 binding behavior of SPOP mutants, NMR experiments were performed (Fig. 2a–f). For wild-type and mutant SPOP proteins, $^{1}H$,$^{15}N$ heteronuclear single quantum coherence (HSQC) NMR spectra were recorded both in unbound form and with 5-fold molar excess of BRD3 (**1**, residues 245–253). The NMR spectra of all mutant proteins demonstrate that the mutations do not disrupt the tertiary fold of the SPOP MATH domain (Fig. S1). Residues Tyr87, Leu88 and Gln127 are key residues directly in the ligand binding site of SPOP. A comparison of the chemical shift perturbation (CSP) of these signals indicates that prostate cancer-associated SPOP mutants show no or very little CSPs upon BRD3 addition (Fig. 2b–c). This demonstrates that these mutants have no or strongly reduced binding affinity to BRD3 compared to the wild-type SPOP protein (Fig. 2a). In contrast, all endometrial cancer-associated SPOP mutants show significant CSPs and line-broadening upon BRD3 addition. The shift patterns of these mutants upon BRD3 addition (Fig. 2d–f) are highly similar to the one of wild-type SPOP, indicating comparable binding modes and strength.

The BRD3 binding affinity of SPOP mutants was also studied by fluorescence polarization measurements. Different concentrations of the respective SPOP proteins were mixed with fluorescently labeled BRD3 peptide (**4**). The binding isotherms of the assay (Fig. 2g) clearly show the different BRD3 binding behavior of endometrial and prostate cancer-associated SPOP mutants. Almost all endometrial cancer-associated mutants show a binding strength to BRD3 comparable to the wild-type protein. Only SPOP R121Q shows slightly reduced binding strength. However, this mutant still binds stronger than all tested prostate cancer-associated mutants. Their binding behavior is significantly reduced compared to the wild-type protein. These observations are consistent with NMR experiments.

To quantitatively determine the binding affinity and thermodynamic features of BRD3 binding, we performed ITC experiments with SPOP proteins (Table S2, Fig.S2). The dissociation constant ($K_D$) of the wild-type SPOP MATH domain to the BRD3 peptide (**1**, residues 245–253) was determined as 168 ± 19 μM. When the most common prostate cancer-associated SPOP mutant F133V [9] was titrated, no binding could be detected. In contrast, all tested endometrial cancer-associated SPOP mutants bind to the BRD3 peptide, with $K_D$ values comparable to SPOP wild-type.

In summary, data from NMR, ITC and fluorescence polarization experiments confirmed that prostate cancer-associated SPOP mutants show no or significantly reduced BRD3 binding, while endometrial cancer-associated SPOP mutants showed binding behavior comparable to wild-type SPOP. None of the mutations caused an increase in binding affinity between SPOP and BRD3.

In order to obtain structural insights into the effects of SPOP MATH mutations, we co-crystallized SPOP MATH E47K, M117 V and D140N with BRD3 (**1**, residues 245–253). The superposition of the co-crystal structures with the wild-type SPOP–BRD3 complex (Fig. 3a) shows almost identical orientation of the SPOP backbone, and highly similar positions of the respective BRD3 ligands. The mutations do not seem to result in an altered SPOP–BRD3 interface, and consistent with our binding studies, there is no structural explanation for the previously postulated increase in affinity for the mutations.

As these data were obtained on a relatively short fragment of BRD3, additional ITC experiments with a longer BRD3 construct (residues 24–416) were performed (Fig.S3) to rule out that additional residues could be involved in the interaction. This BRD3 construct is extended around the SPOP binding site

and comprises both bromodomains of BRD3 and the connecting linker where the degron is localized (Fig. 1a). The titrations showed very similar $K_D$ values of SPOP mutants E47K, E50K, E78K, D140N and R121Q to BRD3, comparable to wild-type SPOP ($K_D$ = 61 ± 11 μM). The affinities to the extended BRD3 protein (24–416) (Table 1, Figs. 3b and S3) are slightly higher than those determined for the BRD3 peptide (**1**, residues 245–253) (Table S2, Fig.S2), indicating that BRD3 residues adjacent to the shorter peptide may provide some contribution to SPOP binding.

Out of all endometrial cancer-associated SPOP mutants, only M117V showed a somewhat

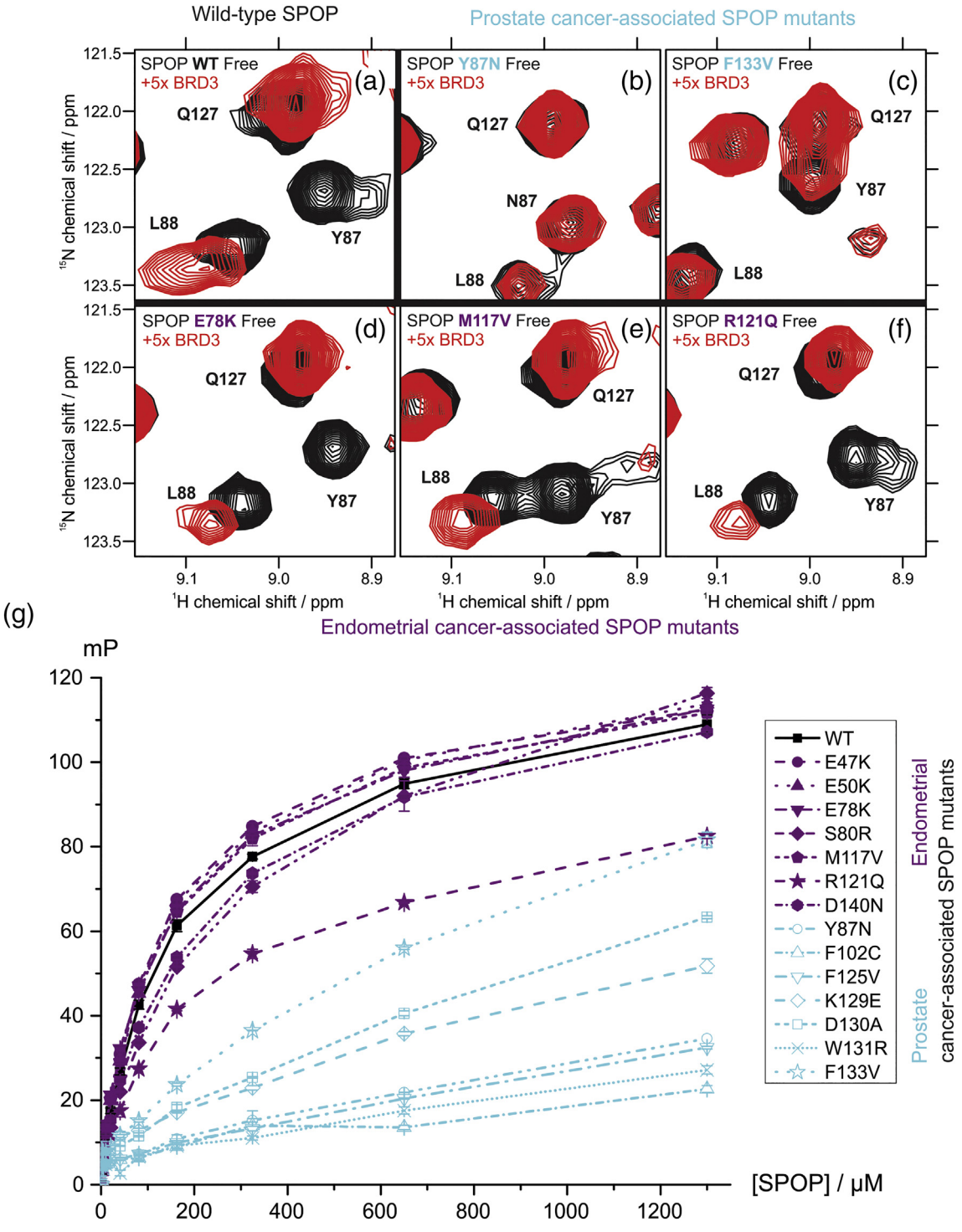

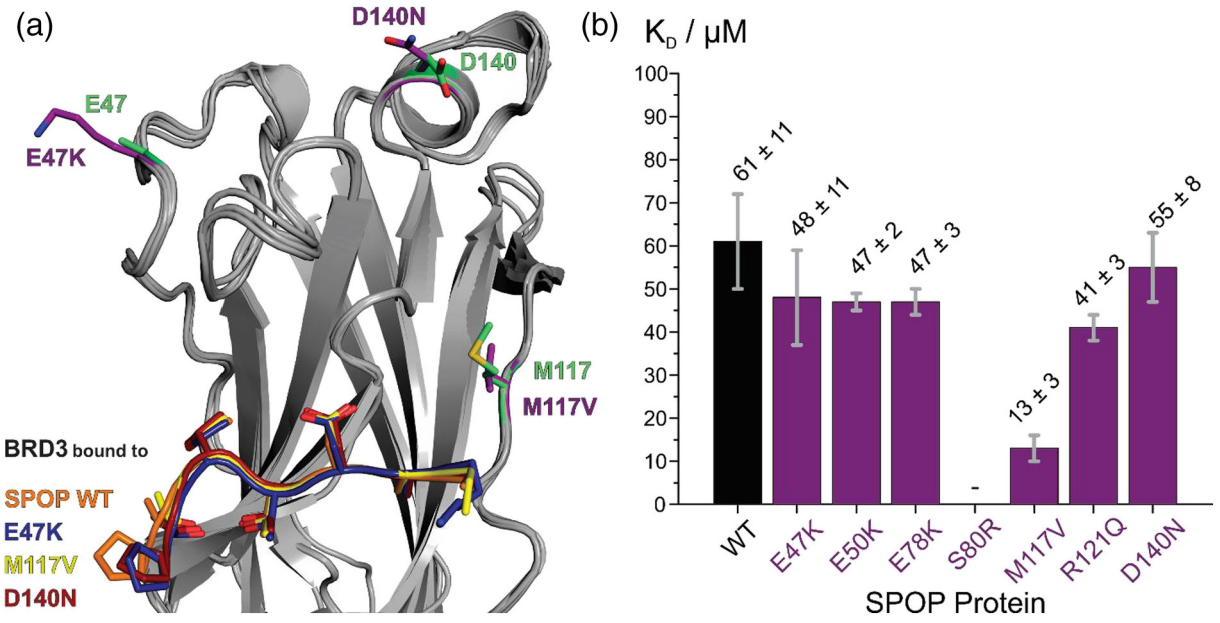


**Fig. 3.** (a) Overlay of co-crystal structures of different SPOP mutants in complex with BRD3. The overlay shows one representative complex for each of the co-crystal structures obtained for SPOP wild-type (WT), E47K, M117 V and D140N with BRD3 (**1**, residues 245–253). SPOP molecules are shown in gray. Mutation sites E47, M117 and D140 in the SPOP WT-BRD3 co-crystal structure are shown as green sticks. In each of the mutant co-crystal structures, the respective mutated residue (K47, V117 or N140) is shown as purple sticks. The BRD3 ligand from all four co-crystal structures is shown as cartoon with side chains (BRD3 from SPOP WT co-crystal structure in orange, from E47K in blue, from M117 V in yellow and from D140N co-crystal structure in red). The overlay shows that all superimposed structures are almost identical in terms of SPOP backbone and BRD3 ligand orientation. This indicates that endometrial cancer-associated mutations E47K, M117 V and D140 do not alter the interface of SPOP MATH to BRD3. (b) Column plot of $K_D$ values obtained from ITC titrations of different SPOP constructs to BRD3. The plot shows the $K_D$ values (*y*-axis) obtained from ITC titrations of different SPOP constructs (*x*-axis) to the BRD3 protein (residues 24–416). Wild-type SPOP is shown in black. Endometrial cancer-associated SPOP mutants are shown in purple. This is a graphical representation of the numbers given in Table 1. For SPOP S80R, no data could be obtained due to sample instability.

increased affinity to the BRD3 protein ($K_D$ = 13 ± 3 µM) compared to wild-type SPOP. As this mutation site is relatively close to the N-terminus of the BRD3 peptide in our co-crystal structure (Fig. 1d), it is conceivable that the residue might be involved in binding to larger BRD3 constructs, implying that the mutation affects the contacts formed distant from the core binding interface. Still, all other tested endometrial cancer-associated mutants showed identical BRD3 binding strength to wild-type SPOP, regardless of the used BRD3 construct.

In conclusion, our data confirm the reduced BRD3 binding capabilities of prostate cancer-associated SPOP mutants, and rationalize the effect of these mutations on a structural level. The mutation sites are located in the ligand binding groove of SPOP and

**Fig. 2.** Biophysical analysis of cancer-associated SPOP mutants binding behavior to BRD3. (a–f) Overlays of $^{1}H,^{15}N$ HSQC NMR spectra of selected SPOP mutants titrated with BRD3. Panels show the reference spectra (free form) in black for the indicated SPOP proteins. Superimposed are spectra recorded after addition of 5× molar excess of BRD3 (**1**, residues 245–253). The wild-type SPOP protein (a) shows clear CSPs indicating binding upon addition of BRD3 in peaks corresponding to residues L88 and Q127. The signal for Y87 is broadened beyond detection. These residues are located directly in the BRD3 binding pocket. Selected prostate cancer-associated SPOP mutants Y87N (b) and F133 V (c) show no or significantly reduced CSPs compared to the wild type, respectively. This indicates severely reduced binding. Contrarily, endometrial cancer-associated SPOP mutants E78K (d), M117 V (e) and R121Q (f) show CSPs comparable to the wild type, indicating similar binding mode and strength. Full spectra are shown in Fig. S1. (g) Fluorescence polarization binding curves of different SPOP mutants to BRD3. SPOP proteins were mixed in a dilution series with fluorescently labeled BRD3 peptide (**4**). Fluorescence polarization values are displayed as mP units. All curves were normalized to 0. The binding curve of wild-type SPOP to BRD3 is shown in black with square ticks. Out of the endometrial cancer-associated mutants (purple curves), mutants E47K, E50K, E78K, S80R, M117 and D140N show binding strength highly similar to the wild type. Only SPOP R121Q of this group shows slightly reduced BRD3 binding. All prostate cancer-associated mutants (cyan curves) show significantly reduced binding to BRD3 compared to SPOP wild type.

**Table 1.** ITC data obtained for titrations of different SPOP constructs to BRD3 protein. The used SPOP proteins (wild-type (black) or endometrial cancer-associated mutants (purple)) are indicated, as well as the used BRD3 construct. $K_D$ is the affinity (dissociation constant), $\Delta H$ is enthalpy, $\Delta G$ is Gibbs free energy, $-T\Delta S$ indicates entropy. n is the number of independent experiments used to calculate values and standard deviations. For SPOP S80R, no data could be obtained due to sample instability. With the exception of M117V, all endometrial cancer-associated SPOP mutants show BRD3 binding behavior highly similar to the wild type.

| SPOP protein | BRD3 construct | $K_D$ (μM) | ΔH (kJ/mol) | ΔG (kJ/mol) | -TΔS (kJ/mol) | n |
|---|---|---|---|---|---|---|
| WT | 24-416 | 61 ± 11 | -95 ± 13 | -24.1 ± 0.4 | 70 ± 13 | 3 |
| E47K | 24-416 | 48 ± 11 | -85 ± 14 | -24.7 ± 0.6 | 61 ± 15 | 3 |
| E50K | 24-416 | 47 ± 2 | -86 ± 2 | -24.7 ± 0.1 | 61 ± 2 | 3 |
| E78K | 24-416 | 47 ± 3 | -92 ± 1 | -24.8 ± 0.1 | 67 ± 1 | 3 |
| S80R | - | - | - | - | - | - |
| M117V | 24-416 | 13 ± 3 | -83 ± 2 | -27.9 ± 0.5 | 55 ± 2 | 6 |
| R121Q | 24-416 | 41 ± 3 | -80 ± 1 | -25.0 ± 0.2 | 55 ± 1 | 3 |
| D140N | 24-416 | 55 ± 8 | -102 ± 8 | -24.4 ± 0.3 | 78 ± 8 | 3 |

are involved in critical contacts. Mutation of any of these residues is thus expected to compromise BRD3 binding. Based on the similarity of different SPOP clients, it is likely that these mutations also impair binding of other SPOP clients [10]. Our work covers most of the known prostate and endometrial cancer-associated SPOP mutation sites. In addition, reported prostate cancer-associated mutation sites include S119 and K134 [9] as well as F101 and K135 [11]. Adjacent SPOP mutation sites were studied in our work (F133, F102). As all of those mutation sites are located in the ligand binding groove, we expect them to have highly similar effects, impairing BET protein binding. As for endometrial cancer-associated SPOP mutants, additional mutation sites P94 [8], E46 [12] and G75 [13] were reported. Again, adjacent mutation sites were studied in our work (E47 and G75), and a similar behavior of the mutants is assumed.

Our studies with endometrial cancer-associated SPOP mutations did neither show an increased binding affinity nor a detrimental effect on the BRD3 binding interface compared to wild-type SPOP. Only when a large BRD3 construct was used as ligand, a single SPOP mutant (M117 V) showed slightly increased affinity in ITC experiments. Based on our structural and biophysical data, it is unlikely that this point mutation could cause the described *in vivo* effect of reduced cellular BRD3 levels in endometrial cancer cells [3]. Moreover, all other mutations do not affect the binding affinity *in vitro*. Therefore, the observed disease phenotypes *in vivo* could be caused by higher-level regulatory mechanisms, where mutations may alter protein localization, bring interactions with additional protein binding partners, or potentially affect liquid–liquid phase-separation of complexes, which were recently shown to be caused by SPOP mutation in cancer cells [14]. Still, in specific tumors, screening for SPOP mutations could offer a vital tool to personalize the therapeutic strategy.

## Materials and Methods

### Protein expression and purification

Human SPOP MATH (residues 28–166) and human BRD3 (24–416) were cloned into pETM-11 vector. SPOP MATH mutants were created using the QuikChange Site-Directed Mutagenesis Kit and Primer Design tool (Agilent Technologies) according to the manufacturer's protocols. Proteins were expressed in *Escherichia coli* BL21 (DE3) cells using ZYM-5052 auto-induction medium. Proteins used for NMR experiments were uniformly labeled with $^{15}N$ or $^{15}N/^{13}C$ by growing expression cultures in M9-based minimal medium. All proteins were purified from cell lysate *via* IMAC using a Ni-NTA column. After elution, proteins were dialyzed to TEV protease cleavage buffer [100 mM Tris–HCl (pH 8.0), 100 mM NaCl, 5 mM β-mercaptoethanol (β-ME)] over night at 4 °C after addition of TEV protease (1:50). After cleavage, proteins were subjected to a second Ni-NTA affinity chromatography step. Proteins were further purified *via* size-exclusion chromatography (SEC) using a HiLoad 16/60 Superdex 75 preparative grade (pg) column (SPOP MATH) or a HiLoad 16/60 Superdex 200 pg column (BRD3) (Äkta system, GE Healthcare). Crystallization buffer [5 mM Tris, 50 mM NaCl, 5 mM β-ME (pH 8.0)] was used as SEC buffer for wild-type SPOP if intended for crystallization. PBS [137 mM NaCl, 2.7 mM KCl, 10 mM $Na_2HPO_4$, 1.8 mM $KH_2PO_4$, 5 mM β-ME (pH 7.4)] was used as SEC buffer for all other samples.

### Crystallization and x-ray structure solution

SPOP MATH (wild-type or mutant protein) was mixed with five-fold molar excess of human BRD3 peptide (**1**, residues 245–253, KADTTTPTT). The mix

was concentrated to 16 mg/ml. The crystallization conditions were as follows: 0.2 M NaCl, 0.1 M Tris (pH 8.5), 25% (w/v) polyethylene glycol (PEG) 3350 (wild type SPOP MATH-BRD3), 0.2 M ammonium acetate, 0.1 M Tris (pH 8.5), 25% (w/v) PEG 3350 (SPOP MATH E47K-BRD3), 0.2 M sodium formate, 0,1 M Bis Tris propane (pH 7.5), 20% (w/v) PEG 3350 (SPOP MATH M117 V-BRD3) and 0.2 M NaCl, 0.1 M Hepes (pH 7.0), 20% (w/v) PEG 6000 (SPOP MATH D140N-BRD3). Crystals grew within 1 to 2 weeks at room temperature in vapor diffusion sitting drops and were frozen using 20% glycerol as cryoprotectant. Crystals were measured at the ID23-2 and ID30A-1 beamlines of the ESRF, Grenoble, France. The obtained data sets were processed using the XDS and XSCALE software [15]. Molecular replacement was performed using Molrep v.11.0 [16]. For the co-crystal structures of SPOP wild type, E47K and M117 V with BRD3, PDB entry 3IVV was used as search model. The search model used for the SPOP D140N–BRD3 co-crystal structure was PDB 6I41. Models were rebuilt using Coot v.0.8.8 [17] and iteratively refined using Refmac5 [18] from the CCP4 suite v.7.0 [19]. Final refinement was done with phenix.refine of the PHENIX suite (v.1.14–3260) [20]. Data collection and refinement statistics are given in Table S1. Structure displays were generated using the PyMol Molecular Graphics System v.1.8.6.0, Schrödinger, LLC. Interactions in crystal structures were analyzed using LigPlot+ v.1.4 [21].

## NMR spectroscopy

NMR titrations were recorded *via* $^{1}H,^{15}N$ HSQC experiments on a Bruker Avance 600 spectrometer equipped with a QCI cryogenic probe at 298 K using Topspin v.3.2 (Bruker BioSpin). Spectra were processed using NMRPipe v.8.9 [22] and analyzed using CCPN Analysis v.2.4.1 [23]. Samples consisted of 100 µM $^{15}N$-labeled SPOP MATH (wild-type or mutant) in PBS (pH 7.4), 10% $D_2O$ and 5 mM β-ME and contained either no ligand (free form) or 5-fold molar excess of BRD3 peptide (**1**). Spectra were recorded using acquisition times of 106.5 ms ($^{1}H$), 60.1 ms ($^{15}N$) with a total duration of 1 h 20 min. For the backbone resonance assignment of SPOP MATH, HNCACB and CBCACONH spectra were used. They were recorded on a Bruker Avance 900 spectrometer equipped with a TCI cryogenic probe at 298 K using Topspin v.3.2 (Bruker BioSpin) and processed and analyzed as mentioned above. The sample consisted of 300 µM $^{15}N/^{13}C$-labeled wild-type SPOP MATH in PBS (pH 7.4), 10% $D_2O$ and 5 mM β-ME. The HNCACB spectrum was recorded with acquisition times of 79.9 ms ($^{1}H$), 24.0 ms ($^{15}N$), 4.2 ms ($^{13}C$) with a total duration of 3d 20 h 38 min. The CBCACONH spectrum was recorded with acquisition times of 79.9 ms ($^{1}H$), 24.0 ms ($^{15}N$), 6.5 ms ($^{13}C$) with a total duration of 3d 1 h 13 min.

## ITC

Titrations were performed using a MicroCal PEAQ-ITC (Malvern) at 25 °C. All samples were dialyzed to identical PBS (pH 7.4) buffer for at least 18 h. Measurements were done with titrant concentrations between 1 and 5.8 mM. Used titrants were SPOP MATH wild-type, E47K, E50K, E78K, M117 V, R121Q, F133 V and D140N. SPOP S80R could not be measured due to sample instability. Cell sample concentrations varied between 50 and 200 µM of BRD3 (**1**, residues 245–253) or BRD3 (residues 24–416). The runs consisted of 19 injections with a volume of 2 µl and a duration of 4 s each. The first injection with a volume of 0.4 µl and a duration of 0.8 s was discarded in the evaluation. The syringe stirring speed was 750 rpm for all runs. The spacing for different runs varied between 120 or 150 s. Raw data were processed and integrated using the MicroCal PEAQ-ITC Analysis Software v.1.0.0.1259 (Malvern). The fitted offset method was used as control during analysis. The resulting values in $\Delta H$/mol were plotted over the molar ratio. The data points were fitted using a one-site binding model based on curve shape and the stoichiometry observed in crystallographic data. All measurements were performed at least in triplicate, as indicated in Tables 1 and S2, respectively.

## Fluorescence polarization assay

A 12-point serial dilution (50% dilution per step) of SPOP MATH proteins was created from a starting concentration of 1.3 mM in PBS (pH 7.4) and 5 mM β-ME, keeping a constant concentration of 40 nM fluorescently labeled BRD3 peptide (**4**). Fluorescence polarization of each sample was measured with an EnVision 2104 Multilabel Plate Reader (PerkinElmer) and the corresponding EnVision Software v.1.12. The data were plotted using OriginPro 9.0G (OriginLab Corp.). Curves were normalized to zero by deduction of blank samples.

## Peptide synthesis

Solid-phase peptide syntheses were performed on a CEM Liberty microwave peptide synthesizer. For 0.1-mmol reaction scale, Fmoc-deprotection was performed by treatment with 10% piperazine (w/v) in ethanol/*N*-methyl pyrrolidinone (10:90) (v/v, 3 ml) under microwave radiation for the first 15 s (155 W, 75 °C) then 50 s (30 W, 90 °C). The peptide resins were then rinsed with dimethyl formamide (3 × 2 ml). Peptide coupling was achieved by addition of a solution containing amino acid (5.0 eq, 0.2 M in dimethyl formamide, 2.5 ml), DIC (5.0 eq, 0.5 M in dimethyl formamide, 1 ml) and Oxyma (5.0 eq, 1 M in dimethyl formamide, 0.5 ml) to the $N^{\alpha}$-deprotected peptide resin and agitated under microwave radiation for first 15 s (170 W, 75 °C) then 110 s (30 W, 90 °C,

vessel under external nitrogen flow). Prior to the cleavage step, the peptide resins were rinsed with dimethyl formamide (2 × 15 ml) and DCM (2 × 15 ml). The cleavage was performed manually by the addition of a mixture of trifluoroacetic acid/triisopropyl silane/water (95:2.5:2.5, % v/v/v; 10 ml) and proceeded within 2–3 h. For the precipitation of the crude product, the cleavage filtrate was treated with diethyl ether (3 × 30 ml).

*Synthesis of Lys-Ala-Asp-Thr-Thr-Thr-Pro-Thr-Thr-$NH_2$*

Lys-Ala-Asp-Thr-Thr-Thr-Pro-Thr-Thr-$NH_2$ (0.1 mmol) was prepared according to the general procedure for peptide synthesis (86%). HRMS (ESI) *m/e* calcd. For $C_{38}H_{68}N_{11}O_{16}$ ($MH^+$) 934.4846, found 934.4854.

*Synthesis of Lys-Ala-Asp-Thr-Thr-Thr-Pro-Thr-Thr-Pra-$NH_2$*

Lys-Ala-Asp-Thr-Thr-Thr-Pro-Thr-Thr-Gly(propargyl)-$NH_2$ (0.1 mmol) was prepared according to the general procedure for peptide synthesis (89%). For introduction of Pra, Fmoc protected propargylglycine was used (Merck) HRMS (ESI) *m/e* calcd. For $C_{43}H_{73}N_{12}O_{17}$ ($MH^+$) 1029.5217, found 1029.5211.

*Synthesis of fluorescein-PEG3-azide*

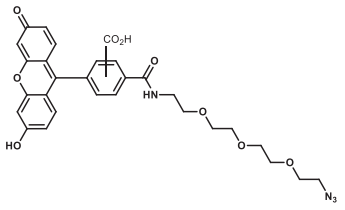


To a solution of 5/6-carboxyfluorescein succinimidyl ester (500 mg, 1.056 mmol, mixture of isomers) in dimethyl formamide (40 ml), diisopropylethyl amine (270 µl, 1.584 mmol, 1.5 eq) and 11-azido-3,6,9-trioxaundecan-1-amine (254 mg, 1.162 mmol, 1.1 eq) were added. The solution was stirred for 14 h at room temperature. The product was purified by HPLC (water + 0.05% trifluoroacetic acid–acetonitrile + 0.05% trifluoroacetic acid; 5%–95% acetonitrile) and obtained as yellow solid (90%). $^1$H-NMR (600 MHz, $CD_3OD$, mixture of isomers) $\delta$ 2.68 (s, 4H), 3.28–3.33 (m, 4H), 3.49–3.71 (m, 30H), 6.53–6.56 (m, 4H), 6.59–6.62 (m, 4H), 6.69 (t, 4H, J = 2.3), 7.33 (dd, 1H, J = 8.0, 0.6, isomer a), 7.65 (dd, 1H, J = 1.4, 0.7, isomer b), 8.08 (dd, 1H, J = 8.0, 0.6, isomer b), 8.15 (dd, 1H, J = 8.1, 1.4, isomer b), 8.21 (dd, 1H, J = 8.0, 1.7, isomer a), 8.44 (dd, 1H, J = 1.5, 0.6, isomer a); $^{13}$C-NMR (600 MHz, $CD_3OD$, mixture of isomers) $\delta$ 26.28, 41.3, 41.24, 51.72, 51.74, 70.27, 70.43, 71.03, 71.11, 71.13, 71.35, 71.43, 71.50, 71.61, 71.64, 71.67, 103.60, 103.61, 110.86, 110.92, 113.67, 123.99, 124.86, 125.66, 126.12, 128.62, 130.13, 130.32, 130.51, 135.57, 137.88, 142.31, 154.03, 168.26, 168.48, 170.59, 174.88; HRMS (ESI) *m/e* calcd. For $C_{29}H_{29}N_4O_9$ ($MH^+$) 577.1935, found 577.1937.

$^1$H and $^{13}$C NMR spectra were obtained on Bruker Ultrashield spectrometer in the indicated solvent. Column chromatography was carried out on a Büchi Reveleris® PREP. HR-MS were measured on a Q-Tof Premier (Waters) with lockspray ion source (ESI, positive ions) coupled to an Acquity UPLC system (Waters). Commercially available chemicals and solvents were used as received.

*Synthesis of Lys-Ala-Asp-Thr-Thr-Thr-Pro-Thr-Thr-Gly($CH_2$-triazol-$PEG_3$-fluorescein)-$NH_2$*

To a solution of **2** (30 mg, 0.019 mmol) in water (8 ml), **3** (20 mM in *tert*. Butanol, 1.0 ml, 0.021 mmol, 1.1 eq) was added. The reaction mixture was degassed by freeze–thaw technique. THTPA (50 mM in water, 0.18 ml, 0.009 mmol, 0.5 eq), copper(II) sulfate (20 mM in water, 0.45 ml, 0.009 mmol, 0.5 eq) and sodium ascorbate (4 mg, 0.019 mmol, 1.0 eq) were added. The solution was stirred for 16 h at room temperature. Organic solvents were removed under reduced pressure, and the product was purified by HPLC (water + 0.05% trifluoroacetic acid–acetonitrile + 0.05% trifluoroacetic acid; 1%–99% acetonitrile). **4** was obtained as yellow solid (33%). HRMS (ESI) *m/e* calcd. For $C_{72}H_{101}N_{16}O_{26}$ ($MH^+$) 1605.7073, found 1605.7068.

**Accession numbers**

Coordinates and structure factors have been deposited in the Protein Data Bank with accession numbers 6I41, 6I5P, 6I68 and 6I7A.

## Acknowledgments

We thank Dr. Arie Geerlof (Protein Expression and Purification Facility, HMGU) for providing materials for protein production. We gratefully acknowledge the use of the X-ray Crystallography Platform (Institute of Structural Biology, HMGU). We thank the European Synchrotron Radiation Facility (Grenoble, France) for beamline access and the Bavarian NMR Center (BNMRZ) for NMR measurement time.

**Author Contributions:** Conception and design of experiments: M.S.O., G.M.P., M.S. Data acquisition and analysis: M.S.O., W.H. Conception and performance of chemical synthesis: W.H., O.P. Writing-original draft: M.S.O., W.H. Writing-review and editing:

O.P., M.S., G.M.P. Project administration and supevision: O.P., G.M.P., M.S.

**Competing Interests Statement:** The authors declare no competing interests.

## Appendix A. Supplementary data

Supplementary data to this article can be found online at https://doi.org/10.1016/j.jmb.2019.04.017.

*Received 8 February 2019;*
*Received in revised form 8 April 2019;*
*Accepted 11 April 2019*
Available online 23 April 2019

***Keywords:***
SPOP;
BET protein;
cancer;
ubiquitination;
x-ray crystallograpgy

†M.S.O. and W.H. contributed equally to this publication.

***Abbreviations used:***
BET, bromodomain and extraterminal; SPOP, speckle-type POZ protein; MATH, meprin and TRAF homology domain; ITC, isothermal titration calorimetry; HSQC, heteronuclear single quantum coherence; CSP, chemical shift perturbation; β-ME, β-mercaptoethanol; SEC, size-exclusion chromatography; PEG, polyethylene glycol; NMR, nuclear magnetic resonance.

## References

[1] M. Perez-Salvia, M. Esteller, Bromodomain inhibitors and cancer therapy: from structures to applications, Epigenetics 12 (2017) 323–339.
[2] X. Dai, et al., Prostate cancer-associated SPOP mutations confer resistance to BET inhibitors through stabilization of BRD4, Nat. Med. 23 (2017) 1063–1071.
[3] H. Janouskova, et al., Opposing effects of cancer-type-specific SPOP mutants on BET protein degradation and sensitivity to BET inhibitors, Nat. Med. 23 (2017) 1046–1054.
[4] P. Zhang, et al., Intrinsic BET inhibitor resistance in SPOP-mutated prostate cancer is mediated by BET protein stabilization and AKT-mTORC1 activation, Nat. Med. 23 (2017) 1055–1062.
[5] M. Zhuang, et al., Structures of SPOP–substrate complexes: insights into molecular architectures of BTB–Cul3 ubiquitin ligases, Mol. Cell 36 (2009) 39–50.
[6] L. Pintard, A. Willems, M. Peter, Cullin-based ubiquitin ligases: Cul3–BTB complexes join the family, EMBO J. 23 (2004) 1681–1687.
[7] M. Furukawa, Y.J. He, C. Borchers, Y. Xiong, Targeting of protein ubiquitination by BTB–Cullin 3–Roc1 ubiquitin ligases, Nat. Cell Biol. 5 (2003) 1001–1007.
[8] M. Le Gallo, et al., Exome sequencing of serous endometrial tumors identifies recurrent somatic mutations in chromatin-remodeling and ubiquitin ligase complex genes, Nat. Genet. 44 (2012) 1310–1315.
[9] C.E. Barbieri, et al., Exome sequencing identifies recurrent SPOP, FOXA1 and MED12 mutations in prostate cancer, Nat. Genet. 44 (2012) 685–689.
[10] M.S. Ostertag, A.C. Messias, M. Sattler, G.M. Popowicz, The structure of the SPOP–Pdx1 Interface reveals insights into the phosphorylation-dependent binding regulation, Structure 27 (2) (2018) 327–334.
[11] M. Blattner, et al., SPOP mutations in prostate cancer across demographically diverse patient cohorts, Neoplasia 16 (2014) 14–20.
[12] S. Jones, et al., Genomic analyses of gynaecologic carcinosarcomas reveal frequent mutations in chromatin remodelling genes, Nat. Commun. 5 (2014) 5006.
[13] P. Zhang, et al., Endometrial cancer-associated mutants of SPOP are defective in regulating estrogen receptor-alpha protein turnover, Cell Death Dis. 6 (2015) e1687.
[14] J.J. Bouchard, et al., Cancer mutations of the tumor suppressor SPOP disrupt the formation of active, phase-separated compartments, Mol. Cell 72 (2018) 19–36 e18.
[15] W. Kabsch, Xds, Acta Crystallogr. D Biol. Crystallogr. 66 (2010) 125–132.
[16] A. Vagin, A. Teplyakov, Molecular replacement with MOLREP, Acta Crystallogr. D Biol. Crystallogr. 66 (2010) 22–25.
[17] P. Emsley, B. Lohkamp, W.G. Scott, K. Cowtan, Features and development of Coot, Acta Crystallogr. D Biol. Crystallogr. 66 (2010) 486–501.
[18] G.N. Murshudov, A.A. Vagin, E.J. Dodson, Refinement of macromolecular structures by the maximum-likelihood method, Acta Crystallogr. D Biol. Crystallogr. 53 (1997) 240–255.
[19] M.D. Winn, et al., Overview of the CCP4 suite and current developments, Acta Crystallogr. D Biol. Crystallogr. 67 (2011) 235–242.
[20] P.D. Adams, et al., PHENIX: a comprehensive Python-based system for macromolecular structure solution, Acta Crystallogr. D Biol. Crystallogr. 66 (2010) 213–221.
[21] R.A. Laskowski, M.B. Swindells, LigPlot+: multiple ligand-protein interaction diagrams for drug discovery, J. Chem. Inf. Model. 51 (2011) 2778–2786.
[22] F. Delaglio, et al., NMRPipe: a multidimensional spectral processing system based on UNIX pipes, J. Biomol. NMR 6 (1995) 277–293.
[23] W.F. Vranken, et al., The CCPN data model for NMR spectroscopy: development of a software pipeline, Proteins 59 (2005) 687–696.